Multiscale and Multidisciplinary Modeling, Experiments and Design (2025) 8:445
https://doi.org/10.1007/s41939-025-01043-3

ORIGINAL PAPER

Using microscale SPH-simulations to parameterize macroscopic fiber orientation models for discontinuous fiber reinforced polymers

Florian Wittemann[1] · **Lukas Hof**[1] · **Luise Kärger**[1]

Received: 16 April 2025 / Revised: 8 September 2025 / Accepted: 10 September 2025

Abstract
The orientation of discontinuous fibers in injection or compression molded parts has crucial impact on the thermo-mechanical properties of the part. Therefore, the prediction of these orientation states is of high importance and has been the focus of research for several years. Today's models often represent the orientation evolution by a semi-empirical tensor evolution equation, which needs at least one empirical parameter. More complex models need more parameters. The determination of these parameters often entails a high experimental effort, especially if data over time is needed. This work presents a multiscale approach, where microscale simulations of individual and interacting fibers in a simple shear flow are used to parameterize macroscopic orientation models. The microscale simulations are performed with the smoothed particle hydrodynamics method. The macroscopic models, being the Folgar-Tucker and ARD-RSC model, are fitted according to the microscale results and are compared to state-of-the-art approaches for parameter determination. For experimental validation, injection molding trials of a 20 weight-% short glass fiber reinforced phenolic are used, showing the benefits of the micro–macro coupling especially when predicting the orientation evolution over time. The main advantage of the multiscale approach is the parameterization of the ARD-RSC approach without the need of experimental data for a wide range of fiber-polymer materials.

Keywords Short fiber reinforced polymers · Micro–macro-coupling · Fiber orientation modeling · Process simulation

1 Introduction

In today's structural and semi-structural applications, discontinuous fiber reinforced polymers (FRPs) become increasingly significant. During manufacturing, for example in injection or compression molding, the material is represented by a fiber-matrix suspension, consisting of the reinforcing fibers and the matrix melt. In this state, the fibers flow within the melt and re-orientate during flow, which makes the material class well suited to manufacture complex geometries. However, this re-orientation significantly affects the thermo-mechanical properties of the final part and is difficult to predict, since many aspects of the process and material must be considered.

Process simulation is an important tool to predict the final fiber orientation and the only possibility to do so without the need of a prototype. At state-of-the-art, process simulations are numerically solved on finite elements or finite volumes in a non-isothermal and transient computational fluid dynamics (CFD) simulation. The fiber matrix suspension is described with a homogenized material modeling approach to keep the simulation numerically capable, and the orientation state is captured by orientation tensors, as presented by (Advani and Tucker 1987). The orientation evolution is mainly dominated by the flow field and, especially for concentrated suspensions, by fiber–fiber interactions (Advani 1994). Today's orientation models are most often based on Jeffery's Equation (Jeffery 1922), describing the rotation of a single ellipsoid in an infinite Newtonian fluid. The first empirical extension of Jeffery's Equation, taking fiber interactions into account, is the Folger-Tucker-Equation (FTE) (Folgar and Tucker 1984). Since then, further extensions are developed to fit to specific material systems, like for example the reduced strain closure model (RSC) (Wang et al. 2008), the anisotropic rotary diffusion model (ARD) (Phelps and Tucker 2009), the

✉ Florian Wittemann
florian.wittemann@kit.edu

[1] Present Address: Institute of Vehicle System Technology, Karlsruhe Institute of Technology (KIT), FAST-LB, Lightweight Engineering Building 70.04, Rintheimer Querallee 2, 76131 Karlsruhe, Germany

Published online: 20 September 2025

combination of the ARD and RSC model, called ARD-RSC model, or the improved anisotropic rotary diffusion model (iARD) (Tseng et al. 2013). The latter was developed mainly because the five empirical parameters needed for the interaction tensor in the ARD approach are hard to determine and the number of parameters is reduced to two in the iARD model. Within (Tucker 2022) it is mentioned, that the ARD(-RSC) approach is often used with the parameters determined in (Phelps and Tucker 2009), although the considered material system is different, since the parameterization includes high experimental effort. Therefore (Tucker 2022) recommends to use a simplification of the ARD approach if a new parameterization is needed. However, these simplified models (i.e. iARD) are of course not as flexible as the ARD approach, which results in restrictions for the modelled orientation behavior. Due to the knowledge of the authors, no non-experimental method to parameterize the ARD-RSC model for a specific material system is presented so far. Several more orientation models with individual (dis-)advantages exist, an overview is given in (Kugler et al. 2020) and (Tseng et al. 2020). The FTE and ARD-RSC model, which are considered in this work, are explained in detail in Sect. 2.2.

The empirical parameters needed in the mentioned macroscopic orientation models can for example be determined by fitting the orientation evolution to experimental data. However, this calls for high experimental effort. Therefore, several studies exist aiming to determine these parameters. In case of the FTE, two of the most common approaches are the ones by (Bay 1991) and (Phan-Thien et al. 2002). Both approaches present an empirical equation, which determines the interaction coefficient C_I for the FTE depending on fiber volume fraction ϕ_f and fiber aspect ratio r_f. It depends on the material system (ϕ_f and r_f) whether (Bay 1991) or (Phan-Thien et al. 2002) is more suitable.

The use of orientation tensors enables the application of orientation models in macroscale simulations to predict orientation states in whole parts. However, this leads to a loss of information, crucial for orientation and structural aspects, such as local geometric changes like ribs. Detailed information about interactions and fiber-flow phenomena may be needed, although only in a few selected areas of a part. Therefore, microscale modeling, meaning the movement and interaction of individual fibers, has been in focus of many scientific publications. In general, such approaches can be separated whether they are single fiber or multiple fiber approaches, if they are one-way (flow influences fiber orientation but not vice-versa) or two-way coupled, or if the fibers are flexible or rigid. An overview is given in (Kugler et al. 2020). The microscale approaches can be compared to macroscale approaches to determine the needed parameters. For example (Mezher et al. 2016) show direct numerical simulations (DNS) of FRPs in confined and unconfined flows. For an unconfined shear flow, the DNS is in good agreement with the macroscale FTE, while the results deviate for confined flows, depending on the closure approximation. (Pérez 2016) developed a finite element based two-way coupled methodology for flow modeling of fiber-matrix suspensions with individual fibers represented as chain of rigid cylinders, taking hydrodynamic and fiber–fiber contact forces into account to determine C_I for the FTE. The orientation states are compared to Jeffery's Equation, FTE and experimental results, showing good agreement. (Meyer et al. 2020) present a two-way coupled microscale approach for FRPs, including fiber–fiber interactions, based on the smoothed particle hydrodynamics (SPH) method. The fibers are represented by a chain of particles. Hence, the initial particle distance Δx is directly related to the fiber diameter d_f. Simulations for simple shear flows are used to quantify C_I and the strain reduction factor κ of the RSC model. Within (Meyer et al. 2020), the orientation over time is considered, not only the steady state solution. (He et al. 2017) present microscale SPH-simulation for injection molding with short fibers and low fiber volume content. To the authors' knowledge, (Meyer et al. 2020) is the only work, fitting data over time for more complex models than the FTE, but with fiber aspect ratios smaller than 5, which is not in the range of common industrial used FRPs.

Within this work, the approach of (Meyer et al. 2020) is adapted and applied for longer fibers and larger model domains, representing an existing FRP. The fiber orientation evolution over time is used in combination with a numerical optimization scheme to parameterize the FTE and ARD-RSC approach. By doing so, a more adequate method to predict orientation states over time is enabled. This offers an advantage for orientation modeling in complex structures with short flow paths, where the fibers do not reach the stationary state and a correct prediction over time is essential.

2 Theory and methods for simulations

2.1 Methods for microscale modeling with individual fibers

The microscale simulations of the fiber reorientation were carried out using the open source SPH-framework *PySPH* (PySPH developers 2025). The SPH method is a Lagrangian method to solve partial differential equations (Lucy 1977; Gingold and Monaghan 1977). The system's mass is discretized as freely movable *particles*. The field variables are interpolated by summation over neighboring particles. For this summation, the particles are weighted according to a smoothing function. There are formulations available allowing both the simulation of fluids and solids. The transfer of forces between solid and liquid phases is handled intrinsically without additional contact algorithms. The method therefore lends itself well to simulate a mixed system such as solid

fibers suspended in a fluid without complex coupling between two solvers or methods.

To simulate the elastic fibers, a method developed by (Meyer et al. 2020) was used. The implementation can be found in a fork of the original project (Meyer 2025). The fibers are each represented by a chain of particles representing a fiber of cylindrical shape. In addition to the forces acting on all fluid particles, the particles belonging to a fiber are subject to additional elastic forces to model the fiber's tensile and bending stiffness (Yang et al. 2014; Meyer et al. 2020). The tensile force $\boldsymbol{F}^{\mathrm{t}}$ between a given particle a and the adjacent particle b is

$$\boldsymbol{F}^{\mathrm{t}}_{ab} = EA\left(\frac{\|\boldsymbol{x}_{ab}\|}{\boldsymbol{x}^{0}_{ab}} - 1\right)\frac{\boldsymbol{x}_{ab}}{\|\boldsymbol{x}_{ab}\|}, \tag{1}$$

where E is the Young's modulus, A is the cross-sectional area of a fiber and $\boldsymbol{x}_{ab}$ is the vector between the particles a and b. The superscript $(\cdot)^0$ denotes the undeformed reference configuration. The bending moment $\boldsymbol{M}^{\mathrm{b}}_{a}$ is

$$\boldsymbol{M}^{\mathrm{b}}_{a} = \frac{EI}{2}\frac{\boldsymbol{\theta}_a - \boldsymbol{\theta}^0_a}{\|\boldsymbol{x}_{a(a-1)}\|+\|\boldsymbol{x}_{a(a+1)}\|}, \tag{2}$$

where I is the second moment of inertia and $\boldsymbol{\theta}_a$ is the enclosed rotation vector between $\boldsymbol{x}_{a(a-1)}$ and $\boldsymbol{x}_{a(a+1)}$. The force $\boldsymbol{F}^{\mathrm{b}}_{ab}$ due to bending is therefore

$$\boldsymbol{F}^{\mathrm{b}}_{ab} = \frac{1}{2}\frac{\boldsymbol{M}^{\mathrm{b}}_{a} \times \boldsymbol{x}_{ab}}{\|\boldsymbol{x}_{ab}\|^2}. \tag{3}$$

The acceleration due to the elastic deformation is the sum of these forces

$$\begin{aligned}\boldsymbol{a}^{\mathrm{elastic}}_{a} = \frac{1}{m_a}\Big(&\boldsymbol{F}^{\mathrm{t}}_{a(a-1)} + \boldsymbol{F}^{\mathrm{t}}_{a(a+1)} + \boldsymbol{F}^{\mathrm{b}}_{a(a-1)} \\ &-\boldsymbol{F}^{\mathrm{b}}_{(a-1)a} + \boldsymbol{F}^{\mathrm{b}}_{a(a+1)} - \boldsymbol{F}^{\mathrm{b}}_{(a+1)a}\Big)\end{aligned} \tag{4}$$

with m denoting the particle mass. The torsional stiffness is neglected. Furthermore, the fibers experience a moment based on the viscous friction acting on their surface (Meyer et al. 2020). Lastly, to avoid penetration of neighboring fibers, contact forces repel fibers close to each other. The contact forces are derived from Hertzian contact between two cylinders (Johnson 1985). The distance of adjacent fibers is found through an algorithm also described in (Meyer et al. 2020).

The fiber orientation tensor found using the microscale model $\widetilde{A}_{ij}$ is calculated from N normalized fiber orientations p_i by (Advani and Tucker 1987)

$$\widetilde{A}_{ij} = \frac{1}{N}\sum_{n=1}^{N}(p_i)_n(p_j)_n. \tag{5}$$

As the elastic fibers can be curved, the orientation of a fiber is calculated as the normalized mean of vectors connecting each fiber particle to the next in the chain.

2.2 Methods for macroscale modeling with orientation tensors

The methods and models for the macroscale simulations are implemented in the open-source finite volume software package *OpenFOAM*. The simulation methodology is described in the previous works (Wittemann et al. 2018, 2019, 2022a, b). Since the focus of this work is on the fiber orientation modeling, the fiber length is assumed to be constant. To model the material flow, the mass balance, momentum balance and energy balance given by

$$\frac{d\rho}{dt} + \frac{\partial(\rho U_i)}{\partial x_i} = 0, \tag{6}$$

$$\frac{d\rho U_i}{dt} + \frac{\partial(\rho U_i U_j)}{\partial x_j} = -\frac{\partial p}{\partial x_i} + \frac{\partial \tau_{ij}}{\partial x_j} \tag{7}$$

$$\frac{d\rho c_{\mathrm{p}} T}{dt} + \frac{\partial\left(\rho c_{\mathrm{p}} U_i T\right)}{\partial x_i} = \lambda\frac{\partial T}{\partial x_i \partial x_i} + \underbrace{\tau_{ij} D_{ij}}_{\text{viscous heat}}, \tag{8}$$

are solved, where x_i is the spatial vector, t the time, ρ the density, U_i the velocity vector, p the pressure, τ_{ij} the viscous stress tensor, c_{p} the specific heat capacity, T the temperature, λ the thermal conductivity and D_{ij} the strain-rate tensor, being the symmetrical part of the velocity gradient. Analogous to the previous work (Wittemann et al. 2019), the viscous stress is calculated by

$$\tau_{ij} = \eta_{ijkl} D_{kl}, \tag{9}$$

with the fourth-order viscosity tensor

$$\begin{aligned}\eta_{ijkl} = &(\eta_{11} - 4\eta_{12} + \eta_{23})A_{ijkl} \\ &+ \left(-\frac{\eta_{11}}{3} + \eta_{23}\right)\left(A_{ij}\delta_{kl} + A_{kl}\delta_{ij}\right) \\ &+ (\eta_{12} - \eta_{23})\left(A_{ik}\delta_{jl} + A_{il}\delta_{jk} + A_{jl}\delta_{ik} + A_{jk}\delta_{il}\right) \\ &+ \left(\frac{\eta_{11}}{9} - \eta_{23}\right)\left(\delta_{ij}\delta_{kl}\right) \\ &+ \eta_{23}\left(\delta_{ik}\delta_{jl} + \delta_{il}\delta_{jk}\right)\end{aligned} \tag{10}$$

for the FRP, where

$$\begin{aligned}\eta_{11} &= \frac{\eta_{\mathrm{M}}\phi_{\mathrm{f}}}{2}\left(\frac{\sqrt{\phi_{\mathrm{f}}/\phi_{\mathrm{fmax}}}}{1-\sqrt{\phi_{\mathrm{f}}/\phi_{\mathrm{fmax}}}}\right)r_{\mathrm{f}}^2, \\ \eta_{12} &= \frac{\eta_{\mathrm{M}}}{2}\left(\frac{2-\sqrt{\phi_{\mathrm{f}}/\phi_{\mathrm{fmax}}}}{1-\sqrt{\phi_{\mathrm{f}}/\phi_{\mathrm{fmax}}}}\right), \\ \eta_{23} &= \frac{\eta_{\mathrm{M}}}{(1-\phi_{\mathrm{f}}/\phi_{\mathrm{fmax}})^2}.\end{aligned} \tag{11}$$

Here, A_{ij} and A_{ijkl} are the second- and fourth-order fiber orientation tensors of the macroscopic orientation model, δ_{ij} is the unity tensor, η_{M} the matrix viscosity and ϕ_{fmax} the maximum possible fiber volume fraction, assuming hexagonal packing of unidirectional orientated fibers with identical diameter, and therefore $\pi/\sqrt{12}$ (Pipes et al. 1991). Equation (11) is originally presented by (Pipes et al. 1991) and Eq. (10) results from orientation averaging of Eq. (11). The procedure is described in detail in (Wittemann et al. 2019) and (Wittemann et al. 2022b).

Within this work, two different approaches for the evolution of fiber orientation in tensorial form are compared. The first is the Folgar-Tucker approach (Folgar and Tucker 1984), given by

$$\begin{aligned}\frac{dA_{ij}}{dt}+\frac{\partial A_{ij}}{\partial x_k}U_k =&-\left(W_{ik}A_{kj}-A_{ik}W_{kj}\right)\\&+\frac{r_{\mathrm{f}}^2-1}{r_{\mathrm{f}}^2+1}\left(D_{ik}A_{kj}+A_{ik}D_{kj}-2D_{kl}A_{klij}\right)\\&+2C_I\dot{\gamma}\left(\delta_{ij}-3A_{ij}\right),\end{aligned}\tag{12}$$

with the vorticity tensor W_{ij}, being the unsymmetrical part of the velocity gradient and $\dot{\gamma}$ the scalar shear rate. Here the empirical interaction coefficient C_{I} can be chosen based on experimental results, experience, phenomenological approaches or, as in this work, microscale simulations. Two popular phenomenological approaches to determine C_{I} are given by (Phan-Thien et al. 2002) with

$$C_{\mathrm{I,PT}}=0.03(1-\exp(-0.224\phi_{\mathrm{f}}r_{\mathrm{f}}))\tag{13}$$

and by (Bay 1991) with

$$C_{\mathrm{I,Bay}}=0.0184\exp(-0.7148\phi_{\mathrm{f}}r_{\mathrm{f}}).\tag{14}$$

According to (Advani 1994), Eq. (13) should be used if $\phi_{\mathrm{f}}r_{\mathrm{f}}<0.1$ and Eq. (14) if $\phi_{\mathrm{f}}r_{\mathrm{f}}\geq 0.1$, which is the case for most commercially available FRPs.

The second orientation model is the ARD-RSC approach (Phelps and Tucker 2009), given by

$$\begin{aligned}\frac{dA_{ij}}{dt}+\frac{\partial A_{ij}}{\partial x_k}U_k =&-\left(W_{ik}A_{kj}-A_{ik}W_{kj}\right)+\frac{r_{\mathrm{f}}^2-1}{r_{\mathrm{f}}^2+1}\\&\left(D_{ik}A_{kj}+A_{ik}D_{kj}-2[A_{ijkl}+(1-\kappa)\right.\\&\left.\left(L_{ijkl}-M_{ijmn}A_{mnkl}\right)]D_{kl}\right)+\dot{\gamma}\left[2\left[C_{ij}\right.\right.\\&\left.-(1-\kappa)M_{ijmn}C_{mn}\right]-2\kappa C_{mn}\delta_{mn}A_{ij}\\&-5\left(C_{ik}A_{kj}+A_{ik}C_{kj}\right)+10\left[A_{ijkl}\right.\\&\left.\left.+(1-\kappa)\left(L_{ijkl}-M_{ijmn}A_{mnkl}\right)\right]C_{kl}\right],\end{aligned}\tag{15}$$

where the interaction tensor C_{ij} is defined as

$$\begin{aligned}C_{ij}=&b_1\delta_{ij}+b_2A_{ij}+b_3A_{ik}A_{kj}\\&+\frac{b_4}{\dot{\gamma}}D_{ij}+\frac{b_5}{\dot{\gamma}^2}D_{ik}D_{kj}.\end{aligned}\tag{16}$$

The strain reduction factor κ is originally introduced in the RSC-model by (Wang et al. 2008), where also the calculation of L_{ijkl} and M_{ijkl} is given. The five empirical constants b_{1-5} and κ will be fitted to the microscale results within this work. For both approaches the fourth-order orientation tensor is approximated with the IBOF5 closure approximation (Du Chung and Kwon 2002). For the fiber aspect ratio r_{f} in the orientation models, an equivalent elliptical aspect ratio is used and according to (Zhang et al. 2011) calculated by

$$\begin{aligned}r_{\mathrm{f\_elip}}=&0.000035r_{\mathrm{f}}^3-0.00467r_{\mathrm{f}}^2\\&+0.764r_{\mathrm{f}}+0.404.\end{aligned}\tag{17}$$

2.3 Parameter optimization scheme

To benefit from the information provided by the microscale simulation in the macroscale simulations, the parameters C_{I} in Eq. (12) as well as κ in Eq. (15) and b_{1-5} in Eq. (16) are determined by fitting Eq. (12) and Eq. (15) to the microscale results. To do so, the fiber orientation evolution according to Eq. (12) and Eq. (15) is determined in *Matlab*, using an explicit solving scheme with a constant time step of 0.025 s. Convergence studies have been performed and this time step was found to be satisfying in quality and effort. Within *Matlab*, Eq. (12) and Eq. (15) are described in a Lagrangian way (not Euler as in the rest of this work). Therefore, the left hand side of Eqs. (12) and (15) is represented by the absolute derivative of time ($dA_{ij}/dt+\partial A_{ij}/\partial x_kU_k$ reduces to dA_{ij}/dt) and no convective term for A_{ij} is determined. Initial orientation, velocity gradient and fiber length have been set constant and according to the microscale simulations described in Sect. 3.2. After a simulation time of 300 s, the results are compared to the macroscale simulation results. The *Matlab* results are interpolated to the time points of the SPH results and the squared error is determined at all time points for each tensor entry individually. Afterwards the mean squared error is calculated and used as optimization goal. Hence, no weighting is applied. To optimize the model parameters, the *Matlab* inbuilt genetic algorithm *GA* is used to find a first solution, afterwards the gradient-based scheme *fminsearch* is used to refine this solution.

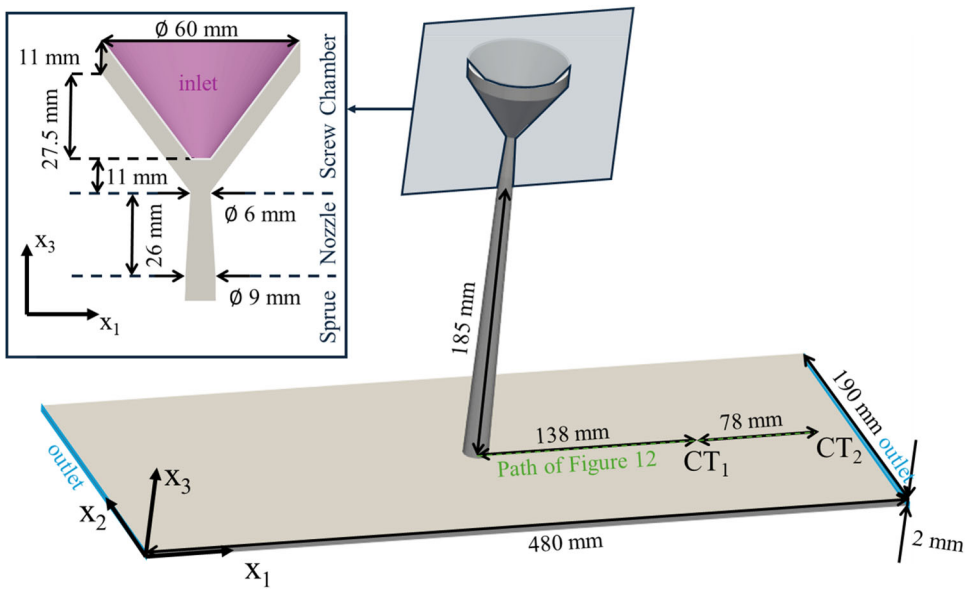

Fig. 1 Plate geometry for experimental trials, including the positions of the CT-Scans CT_1 and CT_2

3 Test cases and experiments

3.1 Experimental setup and trials

To validate the multi-scale fitting approach, macroscale simulations are performed and compared to CT-Scans of experimental trials. The trials are performed with a 20 weight-% (being approximately 10 vol.-%) short glass fiber reinforced phenolic compound. Besides the fiber content, the material is identical to the one regarded in the earlier work (Wittemann et al. 2025), hence, the average fiber length is assumed to be 0.38 mm, corresponding to the values for the SPH simulations (see Sect. 3.2). Further information about the material is given in (Maertens 2022). Plates are manufactured according to the process parameters given in Table 1, the plate geometry and position of CT-specimens is shown in Fig. 1. The positions of CT_1 and CT_2 are at the axis of symmetry, the sprue is placed in the plate's center and has a start and end diameter of 9 mm and 15.5 mm, respectively. The experimental trials have been performed at the Fraunhofer ICT (Pfinztal, Germany) on a KraussMaffei 550/2000 GX equipped with a standard 60 mm thermoset screw without non-return valve. The CT-scans have been performed at the Institute of Applied Materials—Materials Science and Engineering (IAM-WK) at KIT. For every position, three scans out of three plates have been made.

Table 1 Process parameters for injection molding experiments

Parameter	Unit	Value
Melt temperature	°C	120
Mold temperature	°C	175
Injection speed	cm^3/s	50 and 75

3.2 Microscale model setup

SPH particles do not have any particular shape but represent the mass and volume of a cube. The cylindrical fibers are represented as a bead chain of particles and the longitudinal distance of the particles within the chain is set by the initial particle distance Δx. Therefore, it is practical to assume that the fiber particles each represent the volume of a cylinder of the height Δx and the same diameter as the fiber d_f leading to

$$\Delta x^3 = \frac{\pi d_f^2}{4} \Delta x. \tag{18}$$

After rearranging for Δx, the particle distance is set to

$$\Delta x = \frac{\sqrt{\pi}}{2} d_f. \tag{19}$$

The SPH model is set up as a cube of fluid with an edge length 20% longer than the fibers. An exemplary realization is shown in Fig. 2. The domain size strongly influences the computational cost, and no significant difference was observed when comparing the results to those obtained from a larger domain. The same is true for fiber stiffness, which determines the maximum allowable time step. Again, a comparison between fibers with different stiffnesses shows very similar results for stiffnesses higher than the chosen one, see Sect. 4.1 for the relevant results. The number of fibers is calculated to match the desired fiber volume content of 10%. For

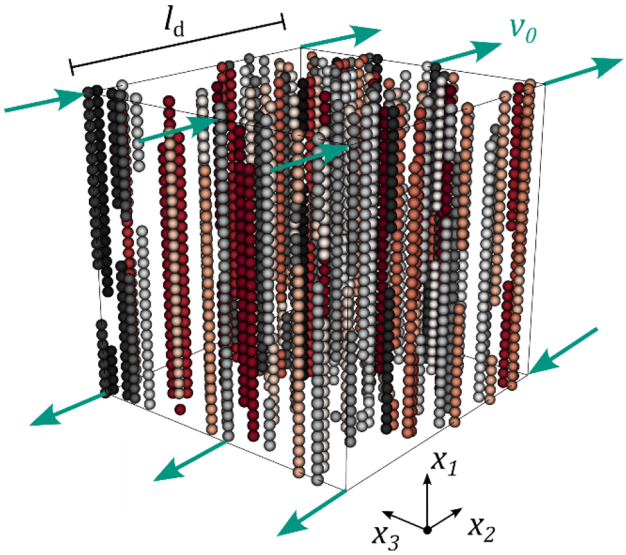

Fig. 2 Exemplary initial configuration of the microscale model of discrete fibers in a shear flow. The fibers are colored for visual distinction. The fluid particles are not displayed

Table 2 Parameters of the microscale model

Parameter	Unit	Value
Global shear rate $\dot{\gamma}$	1/s	1
Fiber volume fraction φ	%	10
Initial particle distance Δx	µm	15.07
Fiber length l_f	µm	376.65
Fiber aspect ratio r_f	-	22.16
Domain length l_d	µm	451.98
Young's modulus of the fibers E	kPa	8462.84
Dynamic Viscosity of the matrix η_M	Pa s	1000
Density of the fluid and fibers ρ	kg/mm^3	10

each necessary fiber, a random start point within the domain is selected and the fibers are extruded along the x_1-axis resulting in a unidirectional initial configuration. To maintain the correct number of particles, fluid particles matching the number of fiber particles are randomly selected and removed. A Lees-Edwards boundary condition (Lees and Edwards 1972) with a velocity $\pm v_0$ along the x_2-axis is applied at both faces of the cube normal to the x_1-axis to induce a constant shear rate $\dot{\gamma}$. Periodic boundary conditions for the velocities are applied to the remaining faces. Fiber ends protruding the boundaries are shifted to the opposite side of the domain in accordance with the periodicity. The setup matches the one described by (Meyer et al. 2020), but with longer fibers and larger simulation domains.

The model parameters are summarized in Table 2. The high physical stiffness of the fibers leads to high accelerations

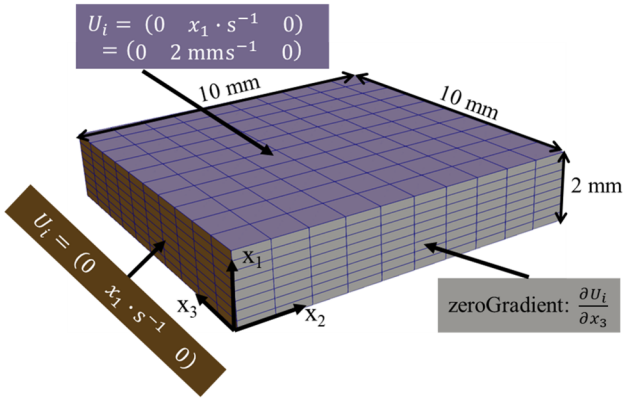

Fig. 3 Macroscale simulation model for comparison to microscale results

from the elastic forces and therefore large displacements within a single timestep. This causes stability issues with the explicit solver used. To allow for feasible timesteps, the stiffness is reduced significantly (Table 2). Parameter studies show very similar results when choosing stiffer fibers or a larger domain respectively, cf. Section 4.1. Both tension and bending stiffness of the fibers are determined by their Young's modulus E. The density ρ is the same across all fiber and fluid particles and scaled up to allow for larger time increments. A constant viscosity η_M is used. The case with the fibers being fully oriented and sheared in 90 degrees is chosen to approximate the transition from sprue to plate (see Fig. 1). The assumption of full orientation is made to simplify the model setup.

3.3 Macroscale model setups

3.3.1 Macroscale model for comparison to microscale model

To compare the fiber orientation evolution in macroscale simulations with the fiber orientation evolution in microscale simulations, a simple rectangular cuboid is regarded in the macroscopic simulations as shown in Fig. 3. The cuboid is meshed with 10 cells in x_2- and x_3-direction and 8 cells in x_1-direction. These cell dimensions are comparable to those in Sect. 3.3.2, used to simulate the plate. Although the flow problem is simple and could be solved with one element, this larger domain is chosen to guarantee that the considered point is in a solved area, where the flow field is determined by the governing equations and not just directly given by the boundary conditions. To realize a simple shear flow, the boundary condition at the walls perpendicular to the x_1-direction is set to $U_i = \left(0 \; x_1 \cdot \mathrm{s}^{-1} \; 0\right)$. This is also the initial condition for the internal velocity field. At the walls perpendicular to

x_2- and x_3-direction, the velocity boundary condition is *zeroGradient,* meaning that the gradients normal to this patch are zero. Therefore, a scalar shear rate of $\dot{\gamma}$=1 1/s is present in the whole domain. Similar to the microscale simulations, the initial fiber orientation is fully oriented in x_1-direction. The fiber volume fraction and fiber aspect ratio are identical to the values given in Table 2. The flow modeling, in particular the calculation of the viscous stress, is performed with anisotropic viscosity (Wittemann et al. 2019).

3.3.2 Macroscale model for comparison to experimental results

To simulate the injection molding process of the experimental trials, the geometry shown in Fig. 1 is meshed and simulated. The cavity is meshed with hexahedral elements. For the plate, the cell size is 2.3 mm in x_1-direction and 1.75 mm in x_2-direction. According to (Wittemann et al. 2019) at least 10 cells should be applied across the plate's thickness, within this work, eleven are used, so that one integration point is exactly in the middle of the plate. The nozzle and sprue is discretized with 32 cells along the circumference, 24 along the diameter and 140 in x_3-direction. Similar to (Wittemann et al. 2025), a part of the screw chamber is also simulated to reach a realistic fiber orientation distribution at the beginning of the sprue. The screw chamber is meshed with 64 cells along the circumference and 72 cells in radial direction, in x_3-direction, the dimension of the cells is 1.57 mm. This results in a simulation domain, containing 313,088 cells. Within the screw chamber, the initial orientation is assumed to be quasi-isotropic. The remaining fiber attributes are identical to Sect. 3.3.1. The process parameters mentioned in Table 1 are applied for the temperature boundary conditions at inlet and walls. The boundary condition for the velocity at the inlet is 50 cm^3/s or 75 cm^3/s and *noSlip* at the walls. For the temperature, it is 120 °C at the inlet and 175 °C at the walls and outlet. The flow modeling is anisotropic and similar to (Wittemann et al. 2019) and (Wittemann et al. 2022a, b) as explained in Sect. 2.1, the matrix viscosity is modeled with the Castro-Macosko model (Castro and Macosko 1982) and the curing kinetics with the Kamal-Sourour approach (Kamal and Sourour 1973).

4 Results and discussion

4.1 Results of the microscale simulations

A parameter study is carried out to identify suitable parameters for the microscale model described in Sect. 2.1. A parameter limiting numerical stability is fiber stiffness. Figure 4 shows the $\widetilde{A}_{11}$-, $\widetilde{A}_{12}$-, $\widetilde{A}_{22}$- and $\widetilde{A}_{33}$-components of the second-order fiber orientation tensor calculated from the micro model for runs with different fiber stiffnesses E. The maximum chosen stiffness of $E \approx 28209$ kPa should depict the behavior of the real fibers with the most accuracy. As expected, Fig. 4 shows, that the reorientation of the fibers differs for low stiffnesses. This is especially evident looking at the first local maximum or minimum: For the three configurations with the lowest stiffnesses this first peak is clearly shifted to the left, while the remaining configurations align well. The orientations later on are more difficult to interpret as the general variation is high, which also depends on the randomness of the initial configuration and will be discussed later in this Section. However, the results are very similar for stiffnesses $E \geq 8463$ kPa. The local minima and maxima of $\widetilde{A}_{11}$, $\widetilde{A}_{12}$ and $\widetilde{A}_{22}$ occur at similar points of time and with similar intensity for $E \geq 8463$ kPa. Based on these results, $E = 8463$ kPa is chosen in the following, as higher stiffnesses are deemed to be too computationally expensive and would therefore limit the number of realizations that can be evaluated.

In a next step, different simulation domain sizes l_d are compared, to guarantee that the model is small and efficient, but also large enough, so that the size does not affect the results. The simulation results for two different l_d are shown in Fig. 5. These two sizes are 1.2 times and 1.5 times the fiber length, which corresponds to 30 and 37 particles along one edge of the cubic domain, respectively. The initial size of 1.2 times the fiber length is chosen, since the domain should be larger than the fiber length, but as small as possible, as the simulations are numerically intensive. Running the model for 300 s as shown in the plots below took roughly 7.3 days on a 16-core CPU. The results in Fig. 5 show, that a larger domain does not significantly change the orientation evolution, since the local minima and maxima are in the same range. Therefore, a domain size of 1.2 times the fiber length creates sufficient results and is used in further simulations.

Finally, different realizations are simulated with $E \approx 8463$ kPa and $l_\mathrm{d} = 451.98$ µm, being 1.2 times the fiber length. Five realizations are shown in Fig. 6. The results differ, since the initial fiber placement is random, although they are orientated in x_1-direction, their initial spatial positions differ in every realization. After a simulation time of 300 s, the values differ by ± 0.015 for $\widetilde{A}_{11}$, by ± 0.012 for $\widetilde{A}_{12}$, by ± 0.045 for $\widetilde{A}_{22}$ and by ± 0.05 for $\widetilde{A}_{33}$. These variations are similar to the variations seen in the parameter study concerning the domain size and similar to the variation between the three results for fibers with higher stiffnesses in the parameter study concerning fiber stiffness, showing that the uncertainty of the stationary state is mainly triggered by the initial configuration. Therefore, the insuppressible uncertainty due to the initial position of the fibers is on the same scale as the deviations of evolution for higher stiffness or larger domains, which again justifies the usage of the chosen parameters.

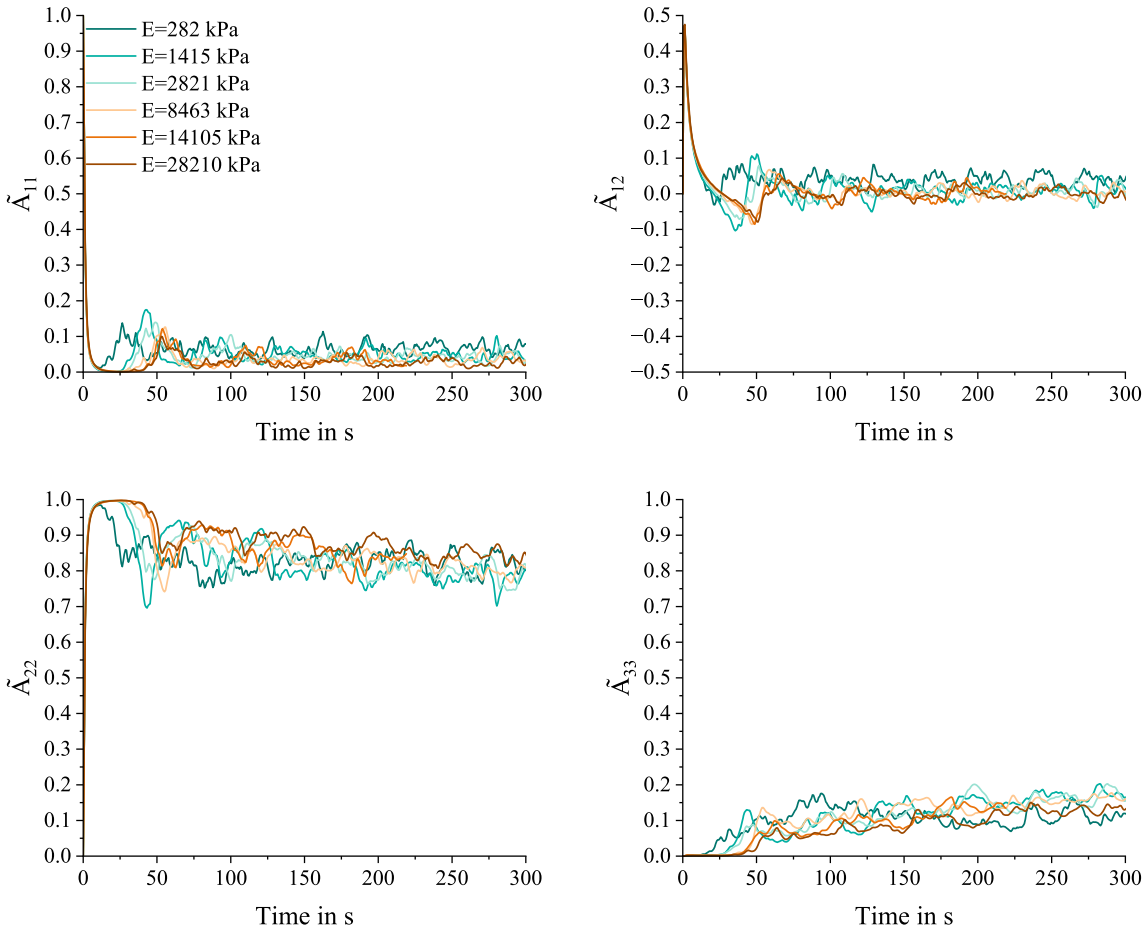

Fig. 4 Comparison of calculated fiber orientation tensor components for different fiber stiffnesses in the SPH simulations

4.2 Comparison of microscale and macroscale simulations

4.2.1 Folgar-Tucker approach with different interaction coefficients

In a next step, the microscale SPH results are compared to the results of macroscale approaches, represented by the evolution of second-order orientation tensors, shown in Fig. 7. For the SPH results (black), the average of five realizations with a fiber stiffness of $E = 8463$ kPa (Fig. 6) is considered, while the corresponding minimum and maximum value are indicated by the grey shading. For the macroscopic results, the Folgar-Tucker approach (Eq. (12)) is compared for different values of C_I, being the two state-of-the-art approaches given in Eq. (13) (PT, red) and Eq. (14) (Bay, orange) and the C_I fitted to the SPH results with procedure explained in Sect. 2.3 (C_I Micro, green). The resulting values are given in Table 3. The results of A_{13} and A_{23} are not shown in Fig. 7, since they are zero for the whole domain in the macroscale approaches.

Compared to the SPH results, the PT and Bay approach reach the stationary state too early, after about 20 s and 50 s. The fitted results reach the stationary state after about 125 s, which is in the range of the SPH results. In general, none of the macroscopic approaches predicts the orientation change of the SPH results for $t < 125$ s, which is especially visible in the local maximum of A_{11} around 60 s in the SPH simulations not being predicted. Additionally, A_{33} rises too early in all three macroscopic approaches, compared to the SPH results. The fitted C_I shows a clear local maximum of A_{11} around 40 s, which is early compared to the SPH-results and shows that the rotation frequency cannot be approximated with the Folgar-Tucker approach. This indicates that for the given ϕ_f=0.1 an RSC-approach might be meaningful, where the strain reduction factor κ lowers the rotation speed. Overall, the fitted approach provides the best results, showing local minima and maxima for A_{11}, A_{12} and A_{22} for $t < 125$ s and fits well to the SPH results for $t > 125$ s, especially for A_{11} and A_{12}.

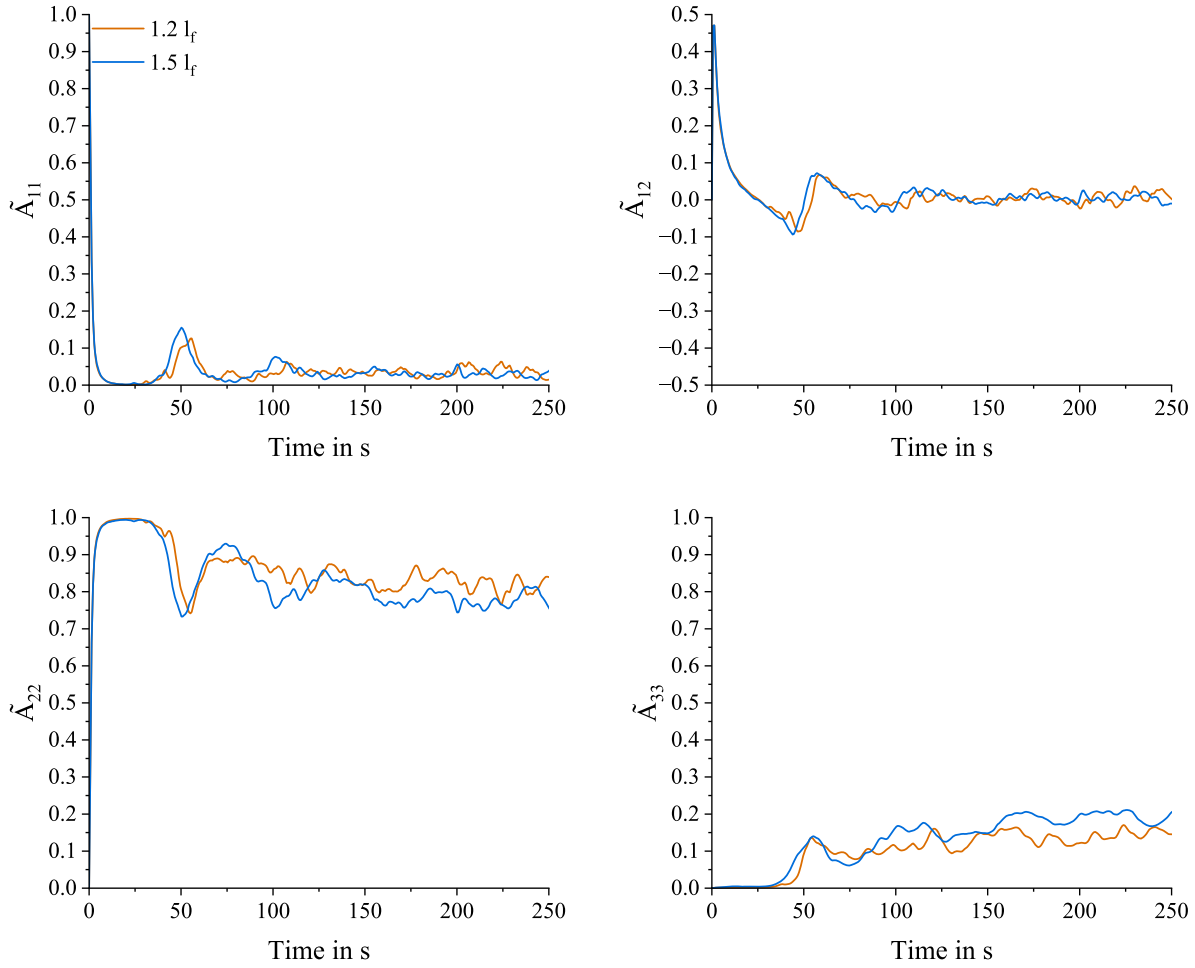

Fig. 5 Comparison of calculated fiber orientation tensor components for different simulation domain sizes in the SPH simulations. The edge length of the cubic simulation domain is 1.2 (red) and 1.5 (blue) times the fiber length

4.2.2 Comparison of Folgar-Tucker and ARD-RSC approach

In a next step, the ARD-RSC approach presented by (Phelps and Tucker 2009) and given in Eq. (15) is fitted to the SPH results. In this approach, six parameters can be fitted. One is the strain reduction factor κ, and the other five are b_{1-5}, which are needed to determine the interaction tensor C_{ij} given in Eq. (16). The need of five parameters for the ARD-model (or six for the ARD-RSC) is one reason, why this model is not often applied or is used with the original parameters given in (Phelps and Tucker 2009), although the material system is different. In this work, the parameter fitting to the SPH simulations is performed with the procedure explained in Sect. 2.3, similar to the Folgar-Tucker approach (Sect. 4.2.1). The resulting parameters are given in Table 4. The resulting orientation tensor evolution is presented in Fig. 8.

As a reference, the Folgar-Tucker results for the fitted C_I are again shown and are identical to Fig. 7. For the Folgar-Tucker as well as for the ARD-RSC model, two different simulation results are shown: firstly, the *Matlab* solution of the evolution equation for a given shear field, as in Fig. 7 (dash-dotted lines), and secondly, the result of *OpenFOAM* simulations as described in Sect. 3.3.1, marked with 'aniso' (dashed lines). The dashed lines are named 'aniso', since the anisotropic approach presented in (Wittemann et al. 2019) is used.

In the simple shear case of this Section, the anisotropic modeling has no detectable influence on the orientation, but this approach is also used for validation in Sect. 4.3, where the anisotropy is more relevant, since the velocity field depends on the anisotropic macroscopic viscosity. The nearly identical results of the explicit solving and *OpenFOAM* confirm the correct implementation of the models in *OpenFOAM*. Compared to the Folgar-Tucker approach, the ARD-RSC approach improves the orientation prediction over the whole

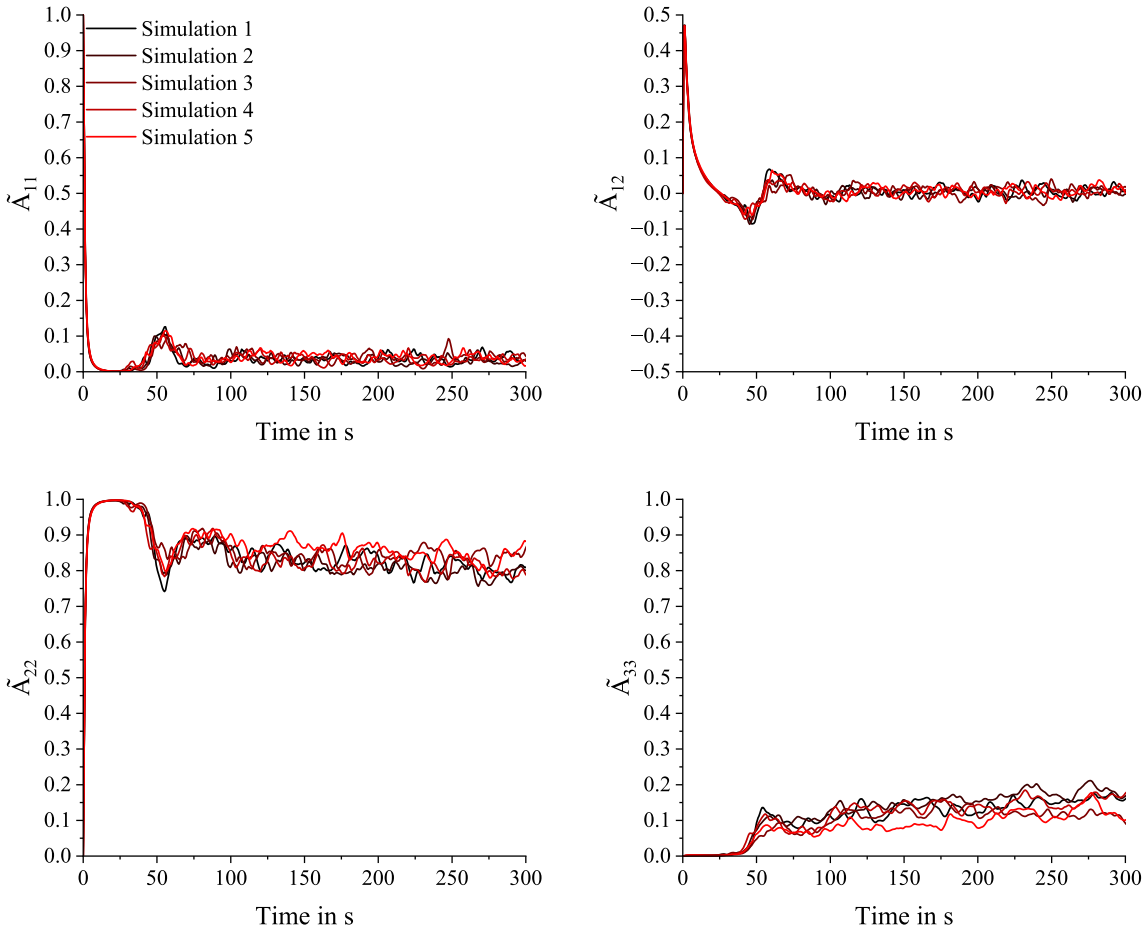

Fig. 6 Comparison of calculated fiber orientation tensor components for different randomly created initial fiber distributions in the SPH simulations

simulation time. The local minima and maxima of A_{11}, A_{12} and A_{22} for $t < 125$ s and also the stationary values of A_{11}, A_{22} and A_{33} are predicted well by the ARD-RSC approach. However, A_{33} being nearly zero for $t < 30$ s is not predicted by the ARD-RSC approach either. According to these results, it is expected that the ARD-RSC model can better predict the re-orientation of the material in the real process compared to the fitted Folgar-Tucker approach. This will be further investigated in the following.

4.3 Comparison of macroscale simulations and experimental data

To validate the parameter identification by microscale simulations with individual fibers for macroscale fiber orientation models, the determined model parameters given in Tables 3 and 4 are used in macroscale injection molding simulations. Detailed information about the injection molding process and material are given in Sect. 3.1, the fiber attributes stay unchanged. The FRP modeling is non-isothermal, non-Newtonian and anisotropic, a detailed description is given in (Wittemann et al. 2019) and Sect. 2.2. Four different approaches are compared, firstly, the Folgar-Tucker approach with C_I according to (Bay 1991) (Eq. (14)), representing the state-of-the-art for the Folgar-Tucker equation and the chosen material system, secondly, the Folgar-Tucker approach with C_I fitted to the microscale results, thirdly the ARD-RSC with the parameters determined in (Phelps and Tucker 2009), named ARD-RSC_SoA (state-of-the-art) and fourthly the ARD-RSC approach with the fitted values from the microscale approach (Table 4), named ARD-RSC_Micro. The state-of-the-art parameters are b_{1-5} =[1.924E-4 5.839E-3 0.04 1.168E-5 0] and κ = 1/30 As mentioned in (Tucker 2022), these values for the ARD-RSC model are often used for different types of FRP materials, since the parametrization is expensive and time consuming. The results of the fiber orientation tensor components A_{11} and A_{22} at the CT scan positions CT_1 and CT_2 are shown in Fig. 9 for an injection speed of 50 cm^3/s and in Fig. 10 for an injection speed of 75 cm^3/s. In Fig. 9b (position CT_2), the two FT and the fitted ARD-RSC approaches create quite similar results with correct tendencies for A_{11}, where the ARD-RSC approach fits slightly better near the surface

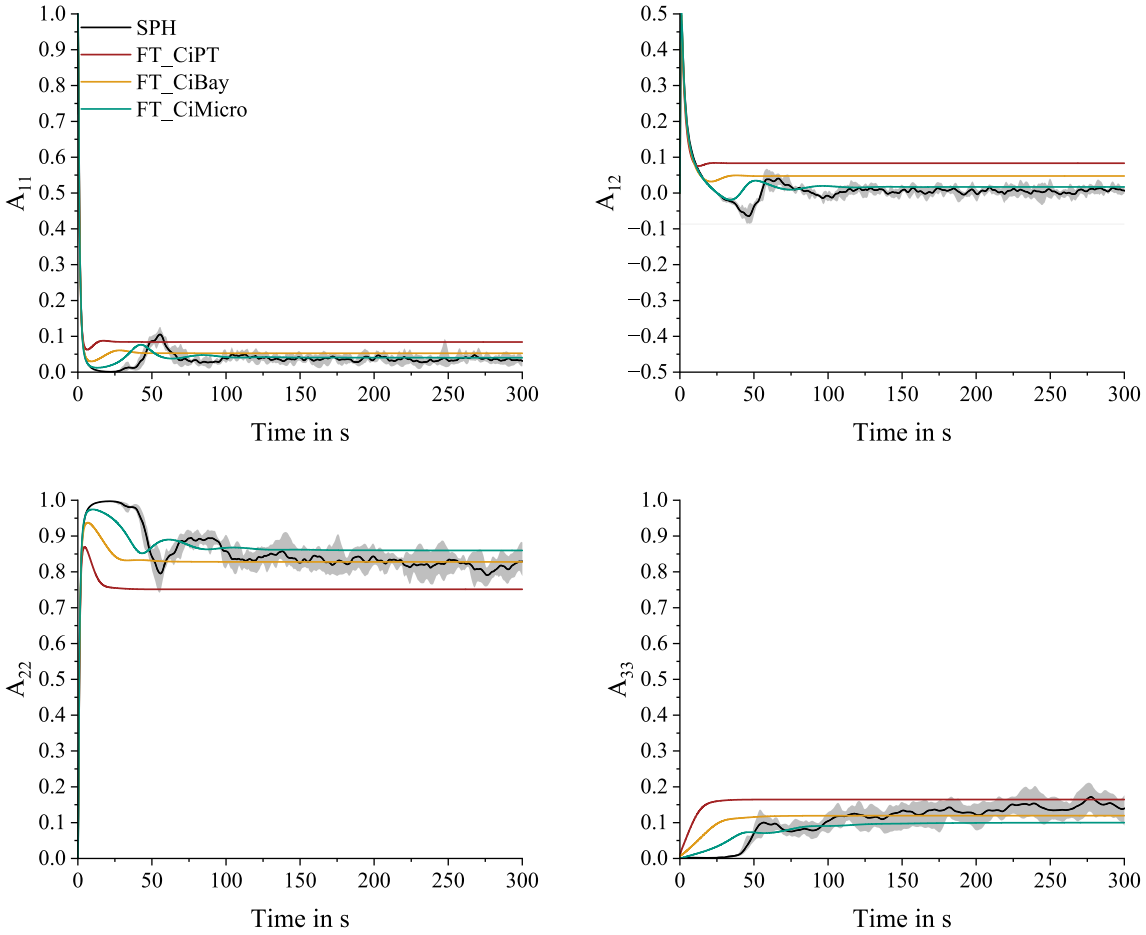

Fig. 7 Comparison of calculated fiber orientation tensor values of SPH simulation (black) and different approaches for C_I in the Folgar-Tucker approach ((Phan-Thien et al. 2002) in red, (Bay 1991) in orange and fitted to SPH results in green)

Table 3 Resulting values of C_I for different approaches

Parameter	Procedure	Value
$C_{I,PT}$	Equation (13)	0.0117
$C_{I,Bay}$	Equation (14)	0.0038
$C_{I,Micro}$	Section 2.3	0.0010

Table 4 Resulting parameters of the ARD-RSC approach

Parameter	κ	b_1	b_2	b_3	b_4	b_5
Value	0.5275	8.2314E-04	2.6519E-12	0.0099	6.5115E-15	2.3331E-14

and in the core. The ARD-RSC_SoA results deviate clearly from the other three, fitting also well to the CT-results in the surface area, but show a too small variation of the orientation over thickness and therefore a too high value of A_{11} in the core, compared to the other approaches and the experimental results. The fitted ARD-RSC prediction of A_{22} is also slightly better close to the surface, but the two FT approaches represent A_{22} better in the core region. This means the fitted ARD-RSC model predicts a higher value of A_{33} which fits to the results shown in Sect. 4.2.2. The ARD-RSC_SoA results again fit also well at the surface for A_{22}, but show very high deviations to the CT-results in the core. The high deviations between the two parameter configurations of the ARD-RSC results highlight the high flexibility but also complexity of this approach, being able to generate such different

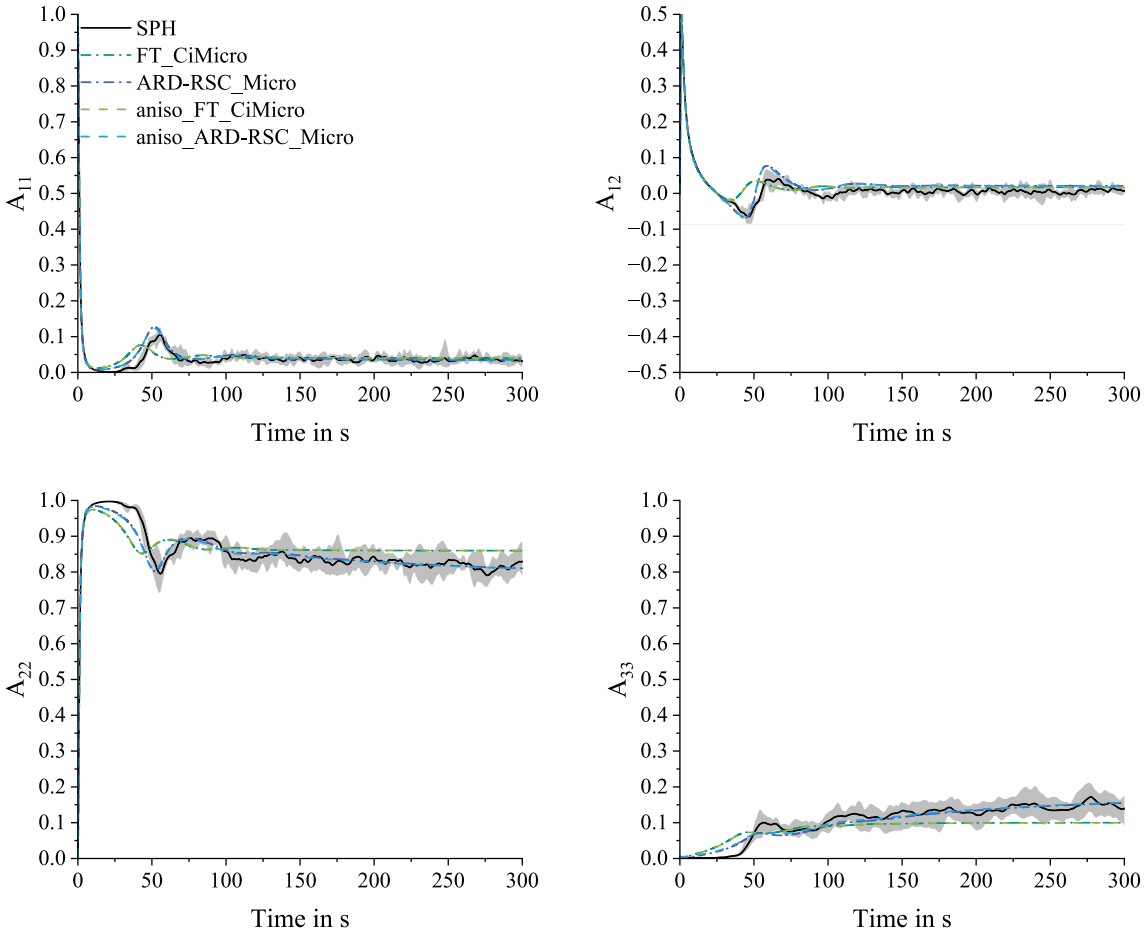

Fig. 8 Comparison of calculated fiber orientation tensor values of SPH simulation (black), fitted Folgar-Tucker approach (green) and fitted ARD-RSC approach (blue). The Folgar-Tucker and the ARD-RSC approach are solved either closely for a given shear field (dark blue and dark green) and by equivalent *OpenFOAM* simulation (light blue and light green)

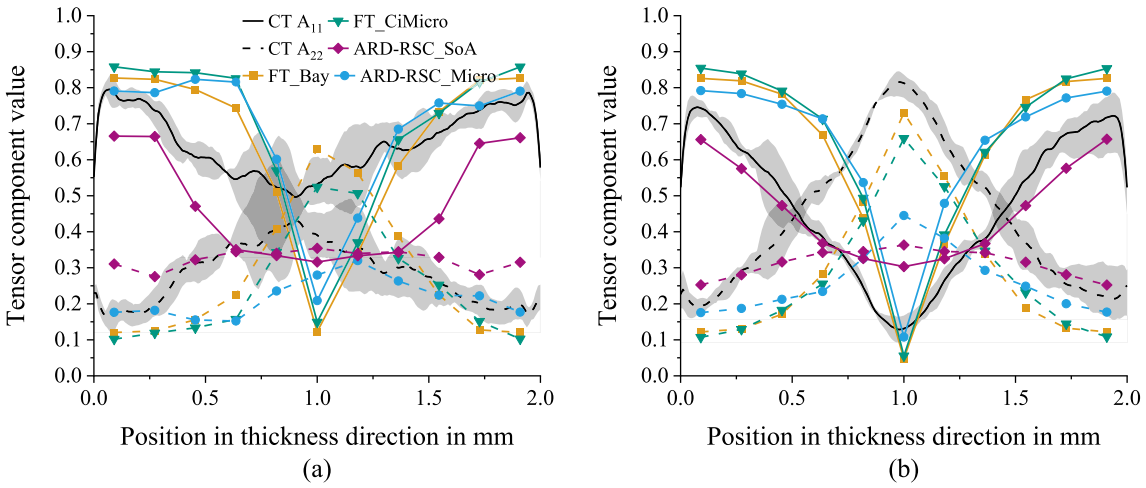

Fig. 9 Comparison of fiber orientation tensor components A_{11} (solid lines) and A_{22} (dashed lines) of macroscale simulations and CT-Scans at position CT_1 (a) and CT_2 (b) (see Fig. 1) for a tool temperature of 175 °C and injection speed of 50 cm^3/s. CT-results in black (including min/max in grey), Folgar-Tucker approach with $C_{I,\,Bay}$ (orange) and fitted C_I (green), the ARD-RSC approach with state-of-the-art parameters (purple) and fitted ARD-RSC approach (blue). A thickness position of 0 mm corresponds to the sprue-side surface (see Fig. 1)

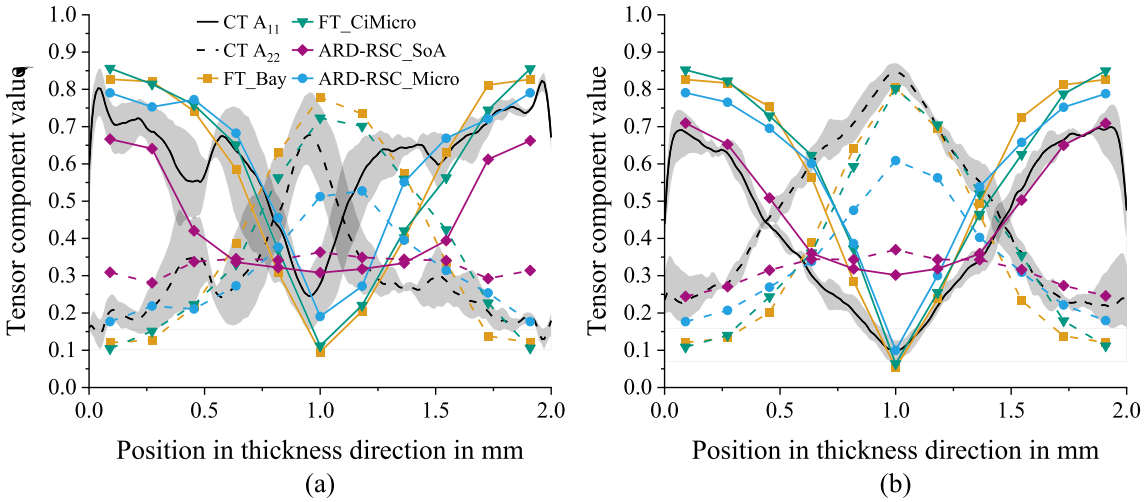

Fig. 10 Comparison of fiber orientation tensor components A_{11} (solid lines) and A_{22} (dashed lines) of macroscale simulations and CT-Scans at position CT_1 (a) and CT_2 (b) (see Fig. 1) for a tool temperature of 175 °C and injection speed of 75 cm.^{3}/s. CT-results in black (including min/max in grey), Folgar-Tucker approach with $C_{I,\,Bay}$ (orange) and fitted C_I (green), the ARD-RSC approach with state-of-the-art parameters (purple) and fitted ARD-RSC approach (blue). A thickness position of 0 mm corresponds to the sprue-side surface (see Fig. 1)

results. This also highlights the importance of a good and efficient possibility to find suitable parameters for the ARD-RSC approach.

In Fig. 9a (position CT_1), all four approaches predict a too low value of A_{11} in the core, while the two Folgar-Tucker approaches also predict a too high value of A_{22} in the core. Again, the ARD-RSC_SoA results show a flatter distribution over plate thickness, compared to the other models. Therefore, the ARD-RSC_SoA results are closer to the CT results of A_{11} in the core region, but worse in surface area and especially in the transition area (around 1.5 mm). The two ARD-RSC approaches are close to the CT results of A_{22} and the fitted one shows a more asymmetric distribution over plate's thickness compared to the Folgar-Tucker approaches. This results from the asymmetric flow field, resulting from the one-sided sprue, being better considered in ARD-RSC approach with the interaction tensor depending on the strain rate tensor, not only on the scalar shear rate. The CT-results in the core region are quite unexpected, showing no intensive drop of A_{11} and are therefore badly predicted by the models, but the scatter in the core region is very high.

The CT results for an injection speed of 75 cm^3/s at CT_2 shown in Fig. 10b are quite similar to the results of an injection speed of 50 cm^3/s, indicating that the flow path is long enough for the fibers to reach their stationary state, which is also supported by the low scatter in both cases. Therefore, the results of the simulation approaches are quite similar, with the fitted ARD-RSC approach creating better results in the surface regions for both tensor components and in the core region for A_{11} and worse results in the core region for A_{22}. The ARD-RSC_SoA approach fits well at the surface regions but shows large deviations in core region for both components and positions. The CT-results in Fig. 10a are more as expected, showing a drop of A_{11} and rise of A_{22}. The CT-results of A_{11} and A_{22} show local minima and maxima in the regions around 0.5 mm and 1.5 mm, which corresponds to the SPH-results for $t < 125$ s (Fig. 6) and indicates, that the stationary state is not yet reached. Although the fitted ARD-RSC approach cannot predict these local minima and maxima, it is the only approach showing a slight non-monotonous progression of A_{11} and A_{22} in the outer region between 0 mm and 0.7 mm. In general, the fitted approaches create meaningful results, showing that the micro-model-based parameter optimization is able to capture different process conditions, although only one shear rate is regarded in the micro models.

To have better comparability, the mean squared error (MSE) between the CT-scans and the respective approaches is calculated. The MSE is the mean of eleven points along the plate's thickness, represented by the cell centers of the simulation mesh. The MSEs are shown in Fig. 11 for an injection speed of 50 cm^3/s (Fig. 11a) and 75 cm^3/s (Fig. 11b). It should be mentioned, that the MSE results should not be evaluated isolated from the results in Figs. 9 and 10, since the information about distribution over plate thickness vanishes.

The ARD-RSC_SoA shows the highest spectrum of occurring MSEs, including lowest and highest values, making it hard to evaluate the quality of the results. The fitted ARD-RSC approach shows the lowest values (A_{11} and A_{22} in sum) for both CT_1 (50 cm^3/s and 75 cm^3/s), which highlights the benefit of the micro model-based fitting, being able to predict the orientation over time and not only for stationary states. Furthermore, the high differences between the two

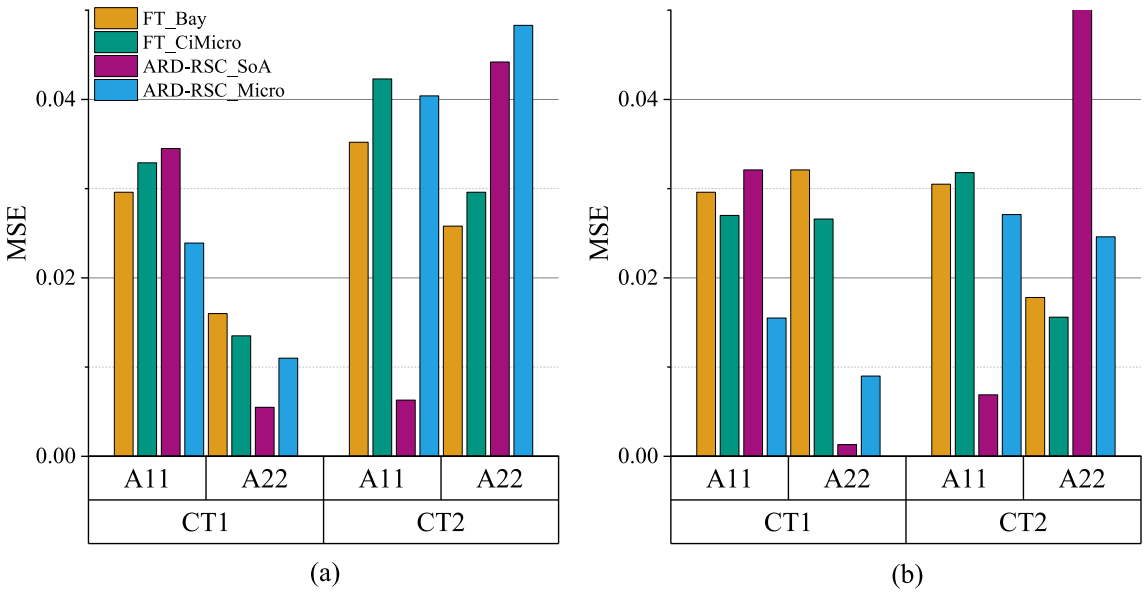

Fig. 11 Calculated mean squared error for tensor values and CT positions corresponding to the results shown in Fig. 9 for a tool temperature of 175 °C and injection speed of 50 cm^3/s (**a**) and 75 cm^3/s (**b**). Folgar-Tucker approach with $C_{I,\,Bay}$ (orange) and fitted C_I (green), the ARD-RSC approach with state-of-the-art parameters (purple) and fitted ARD-RSC approach (blue)

ARD-RSC results and the low MSE of ARD-RSC_SoA for A_{22} at CT_1 and A_{11} at CT_2 shows the flexibility of the model, due to the six independent parameters.

To have a better evaluation of the flow behavior over time for the different approaches and parameters, Fig. 12 shows results along the flow path of the plate. The shown range starts at the center of the sprue and ends at CT_2 (see Fig. 1). The values of A_{11} and A_{22} right underneath the sprue-side surface, in the top row of finite volumes (Fig. 12a), and in the midplane of the plate (Fig. 12b) are displayed. The small change between CT_1 and CT_2 in the experimental results near the surface indicates a stationary state, which is not the case in the midplane. The stationary state is reached faster near the surface due to the higher shear rates. Similar to the pure shear results in Sect. 4.2, the models show local minima and maxima before reaching a stationary state (Fig. 12a up to 40 mm), which is not the case for the ARD-RSC_SoA results. The local peaks are higher for the micro fitted Folgar-Tucker and ARD-RSC approach, while the FTE with C_I from Bay reaches the stationary state with a nearly monotonous progression of A_{11} and A_{22}. The high changes of the ARD-RSC_SoA approach between CT_1 and CT_2 indicate, that the stationary state is not reached near the wall, which does not fit to the experimental results. In the midplane (Fig. 12b), the peaks of the two FT and the fitted ARD-RSC approaches are quite similar, while the results at the end of the flow path differ considerably. In general, none of the approaches creates good results between 138 mm and 216 mm. However, the two FT and the fitted ARD-RSC approaches show the correct tendency, being a rising A_{22} and a decreasing A_{11}, while the ARD-RSC_SoA stay nearly constant along the complete path.

In Summary, the comparison to the experimental results shows, that the approach of (Bay 1991), being quite simple and efficient, creates adequate results for the given material system, especially after a long flow path. However, this approach seems to be not well suited for short flow paths, since the fibers reach a stationary orientation state quite fast and monotonously. Here, the fitted approaches and especially the ARD-RSC approach create more realistic results, which come along with higher numerical effort to determine the parameters. Additionally, the ARD-RSC creates the best results near the surface for both parameter configurations, being the most important region for the bending behavior of a part. The different behavior of the ARD-RSC model for the different parameters shows the high flexibility of model which suits it to be applied for multiple fiber-polymer suspensions. However, the six independent parameters are expensive to determine and as shown, choosing wrong parameters may have high impact. Therefore, the presented fitting on micro simulation results is highly beneficial to parameterize this approach for different materials without need of experiments. Nevertheless, the predicting of material behavior can be improved, so further investigation in the micro model and understanding of the phenomena in the material on micro scale are needed.

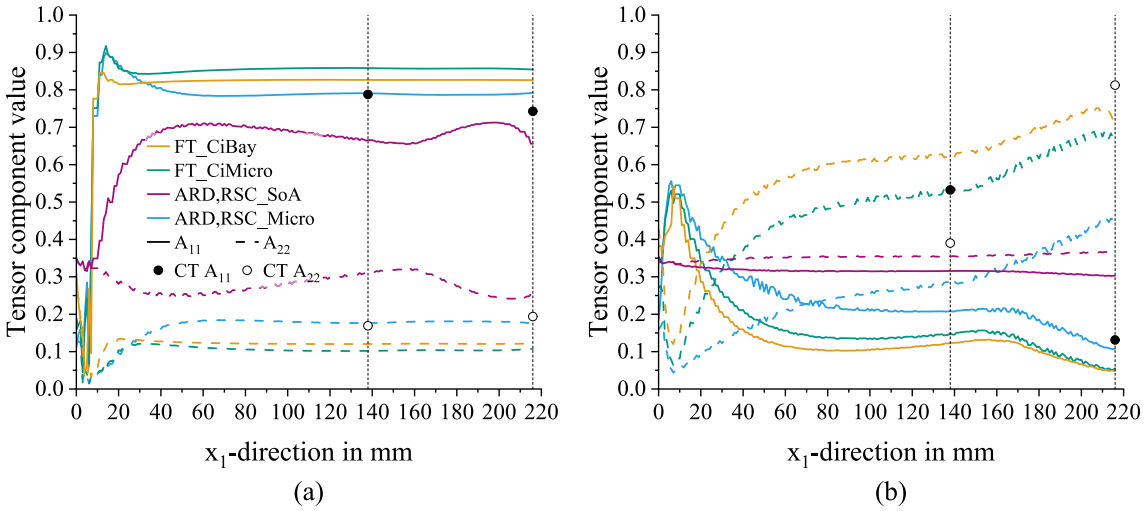

Fig. 12 Comparison of fiber orientation tensor components A_{11} (solid lines) and A_{22} (dashed lines) along the flow path, 0.09 mm below the sprue-side surface (a) and at the midplane (b) for $x_2 = 0$ mm (see Fig. 1). Tool temperature is 175 °C and injection speed 50 cm^3/s. CT results in black (full circle for A_{11} and empty circle for A_{22}), Folgar-Tucker approach with $C_{I,Bay}$ (orange) and fitted C_I (green), the ARD-RSC approach with state-of-the-art parameters (purple) and fitted ARD-RSC approach (blue). x_1-direction of zero corresponds to the center of the sprue (see Fig. 1)

5 Conclusion

The present work presents and discusses a possibility to parameterize fiber orientation evolution models for macroscopic flow simulations of short fiber reinforced polymers. The basis for these parameterizations are SPH simulations, representing microscopic modelling domains with individual and interacting fibers in a simple shear field. The micro model is based on the work of (Meyer et al. 2020), but for larger domains and longer fibers. Furthermore, it is used to fit more complex macroscopic models in this work and is compared to experimental results. Simple shear simulations are evaluated over time, and the second-order fiber orientation tensor is calculated for the whole domain and compared to results of macroscopic simulations. This comparison is used to fit the interaction coefficient of the Folgar-Tucker approach and the strain reduction factor and interaction tensor of the ARD-RSC model. The fitted parameters are used in macroscopic injection molding simulations of a plate geometry. The simulation results are compared to simulation results with state-of-the-art model parameters as well as to CT-Scans of experimental injection molding trials with a 20 %-weight glass fiber reinforced phenolic. The results show that the state-of-the-art methods to determine the interaction coefficient of the Folar-Tucker approach are well suited to predict the stationary orientation state. However, to predict the orientation state within the part, before reaching a stationary state adequately, the ARD-RSC approach is needed. This is supported by the CT-results and the fact that the ARD-RSC approach is the only one that is able to capture the SPH results over the whole time. The high flexibility of the ARD-RSC approach, but also the sensitivity to its model parameters, is demonstrated by comparing the micro-fitted parameters to often used parameters from literature. The ARD-RSC model needs six empirical parameters, which necessitates high experimental effort, if they must be identified experimentally, especially over time or flow path. Therefore, the microscopic approach is beneficial, as it gives time-dependent data, which can be used to parameterize such a complex orientation model as the ARD-RSC model. The multiscale approach thus enables the usability of the ARD-RSC model for a wide range of material systems, solely by means of virtually determined model parameters and without extensive experimental testing.

Acknowledgements We would like to thank the 'Deutsche Forschungsgemeinschaft' (DFG) for funding the research project 'MeproSi' (project number: 464119659), which enabled this work. The work is also part of the Heisenberg project "Digitalization of fiber-reinforced polymer processes for resource-efficient manufacturing of lightweight components", funded by DFG (project no. 798455807141).

Author contributions Florian Wittemann performed the major part of the work in terms of method development and implementation. He also wrote the first draft of the paper. Lukas Hof performed the SPH-simulations and wrote the first draft of Sect. 2.1 and 3.2. Luise Kärger supervised the method development, supported the discussion of simulation results and thoroughly revised the paper.

Funding Open Access funding enabled and organized by Projekt DEAL. This work was enabled by the 'Deutsche Forschungsgemeinschaft' (DFG) by funding the research project 'MeproSi' (project number: 464119659). The work is also part of the Heisenberg project

"Digitalization of fiber-reinforced polymer processes for resource-efficient manufacturing of lightweight components", also funded by DFG (project no. 798455807141).

Data availability No datasets were generated or analysed during the current study.

Declarations

Competing interests The authors declare no competing interests.

References

Advani SG (1994) Flow and rheology in polymer composites manufacturing. Elsevier, Amsterdam; New York

Advani SG, Tucker CL (1987) The use of tensors to describe and predict fiber orientation in short fiber composites. J Rheol 31:751–784. https://doi.org/10.1122/1.549945

Bay R (1991) Fiber orientation in injection molded composites: a comparison of theory and experiment. University of Illinois, Urbana-Campaign

Castro JM, Macosko CW (1982) Studies of mold filling and curing in the reaction injection molding process. Am Inst Chem Eng J 28:250–260. https://doi.org/10.1002/aic.690280213

Du Chung H, Kwon TH (2002) Invariant-based optimal fitting closure approximation for the numerical prediction of flow-induced fiber orientation. J Rheol 46:169–194. https://doi.org/10.1122/1.1423312

Folgar F, Tucker CL (1984) Orientation behavior of fibers in concentrated suspensions. J Reinf Plast Compos 3:98–119

Gingold RA, Monaghan JJ (1977) Smoothed particle hydrodynamics: theory and application to non-spherical stars. Mon Not R Astron Soc 181:375–389. https://doi.org/10.1093/mnras/181.3.375

He L, Lu G, Chen D et al (2017) Three-dimensional smoothed particle hydrodynamics simulation for injection molding flow of short fiber-reinforced polymer composites. Modelling Simul Mater Sci Eng 25:055007. https://doi.org/10.1088/1361-651X/aa6dc9

Jeffery GB (1922) The motion of ellipsoidal particles immersed in a viscous fluid. Proc R Soc London 102:161–179

Johnson KL (1985) Contact mechanics, 1st edn. Cambridge University Press

Kamal MR, Sourour S (1973) Kinetics and thermal characterization of thermoset cure. Polym Eng Sci 13:59–64. https://doi.org/10.1002/pen.760130110

Kugler SK, Kech A, Cruz C, Osswald T (2020) Fiber orientation predictions—a review of existing models. J Compos Sci 4:69. https://doi.org/10.3390/jcs4020069

Lees AW, Edwards SF (1972) The computer study of transport processes under extreme conditions. J Phys C Solid State Phys 5:1921–1928. https://doi.org/10.1088/0022-3719/5/15/006

Lucy LB (1977) A numerical approach to the testing of the fission hypothesis. Astron J 82:1013. https://doi.org/10.1086/112164

Maertens R, Karlsruher Institute of Technology (2022) Process Development and Material Characterization for the Injection Molding of Long Glass Fiber-Reinforced Phenol Formaldehyde Resins: Doctoral Thesis. Karlsruher Institut für Technologie (KIT), Karlsruhe, Germany

Meyer N (2025) PySPH: a python-based SPH framework

Meyer N, Saburow O, Hohberg M et al (2020) Parameter identification of fiber orientation models based on direct fiber simulation with smoothed particle hydrodynamics. J Compos Sci 4:77. https://doi.org/10.3390/jcs4020077

Mezher R, Perez M, Scheuer A et al (2016) Analysis of the Folgar & Tucker model for concentrated fibre suspensions in unconfined and confined shear flows via direct numerical simulation. Compos Part A Appl Sci Manuf 91:388–397. https://doi.org/10.1016/j.compositesa.2016.10.023

Pérez C (2016) The use of a direct particle simulation to predict fiber motion in polymer processing. University of Wisconsin-Madison, Madison, Wis

Phan-Thien N, Fan X-J, Tanner RI, Zheng R (2002) Folgar-tucker constant for a fibre suspension in a Newtonian fluid. J Non-Newton Fluid Mech 103:251–260. https://doi.org/10.1016/S0377-0257(02)00006-X

Phelps JH, Tucker CL (2009) An anisotropic rotary diffusion model for fiber orientation in short- and long-fiber thermoplastics. J Non-Newton Fluid Mech 156:165–176. https://doi.org/10.1016/j.jnnfm.2008.08.002

Pipes RB, Hearle JWS, Beaussart AJ et al (1991) A constitutive relation for the viscous flow of an oriented fiber assembly. J Compos Mater 25:1204–1217. https://doi.org/10.1177/002199839102500907

PySPH developers (2025) PySPH: a python-based SPH framework

Tseng H-C, Chang R-Y, Hsu C-H (2013) Phenomenological improvements to predictive models of fiber orientation in concentrated suspensions. J Rheol 57:1597–1631. https://doi.org/10.1122/1.4821038

Tseng H-C, Chang R-Y, Hsu C-H (2020) Comparison of recent fiber orientation models in injection molding simulation of fiber-reinforced composites. J Thermoplast Compos Mater 33:35–52. https://doi.org/10.1177/0892705718804599

Tucker CL (2022) Fundamentals of fiber orientation: description, measurement and prediction. Hanser Publishers, Munich

Wang J, O'Gara JF, Tucker CL (2008) An objective model for slow orientation kinetics in concentrated fiber suspensions: theory and rheological evidence. J Rheol 52:1179–1200. https://doi.org/10.1122/1.2946437

Wittemann F, Maertens R, Bernath A et al (2018) Simulation of reinforced reactive injection molding with the finite volume method. J Compos Sci 2:5. https://doi.org/10.3390/jcs2010005

Wittemann F, Maertens R, Kärger L, Henning F (2019) Injection molding simulation of short fiber reinforced thermosets with anisotropic and non-Newtonian flow behavior. Compos Part A Appl Sci Manuf 124:105476. https://doi.org/10.1016/j.compositesa.2019.105476

Wittemann F, Kärger L, Henning F (2022a) Influence of fiber breakage on flow behavior in fiber length- and orientation-dependent injection molding simulations. J Non-Newton Fluid Mech 310:104950. https://doi.org/10.1016/j.jnnfm.2022.104950

Wittemann F, Karlsruher Institute of Technology (2022b) Fiber-dependent injection molding simulation of discontinuous reinforced polymers: Doctoral Thesis. KIT Scientific Publishing, Karlsruhe, Germany

Wittemann F, Krauß C, Kärger L (2025) Efficient approximation of varying fiber orientation states in injection molded parts under consideration of multiple manufacturing uncertainties. Appl Compos Mater 32:149–172. https://doi.org/10.1007/s10443-024-10268-3

Yang X, Liu M, Peng S (2014) Smoothed particle hydrodynamics and element bending group modeling of flexible fibers interacting with viscous fluids. Phys Rev E 90:063011. https://doi.org/10.1103/PhysRevE.90.063011

Zhang D, Smith ED, Jack AD, Montgomery-Smith S (2011) Numerical evaluation of single fiber motion for short-fiber-reinforced composite materials processing. J Manuf Sci Eng 133:051002. https://doi.org/10.1115/1.4004831